PHYSICAL REVIEW B **105**, 144108 (2022)

Role of point defects in stress-induced martensite transformations in NiTi shape memory alloys: A molecular dynamics study

Chao Yang* and Janelle P. Wharry
School of Materials Engineering, Purdue University, West Lafayette, Indiana 47906, USA

(Received 24 November 2021; accepted 14 April 2022; published 25 April 2022)

Shape-memory properties of equiatomic NiTi rely on the thermal- or stress-induced reversible martensitic phase transformation between the $B2$ and $B19'$ phases. Irradiation defects suppress thermal-induced transformations, but their effects on stress-induced transformations are poorly understood. We use molecular dynamics to investigate the effect of vacancies, vacancy clusters, interstitials, and antisite defects on stress-induced transformations. All defects suppress the transformation, but vacancy clusters do so to the greatest extent, while antisite defects do so to the least extent. The responsible mechanisms are grain boundary pinning and chemical disordering.

DOI: 10.1103/PhysRevB.105.144108

I. INTRODUCTION

Nitinol (Ti-Ni at approximately equal atomic percentages) draws considerable interest due to its unique properties such as the shape memory effect, superelasticity (pseudoplasticity), excellent corrosion resistance, and high damping capacity [1,2]. These properties place nitinol among the next-generation materials for the defense, nuclear, and aerospace industries [3,4]. Stable mechanical performance under extreme environments such as irradiation are required for these applications. Thus, researchers have studied the microstructural evolution and mechanical behaviors of nitinol alloys under neutron [5–12], proton [13–22], ion [23–25], and electron irradiation [26,27], with an emphasis on thermally and/or stress-induced martensite transformation, which is the origin of the shape memory effect and superelasticity.

For thermally induced martensite transformation, Hoshiya *et al.* [5,6,8] report a significant drop of the martensite start temperature (M_s) of NiTi under different energies, doses, and temperatures of neutron irradiation using electrical resistance measurements. The decrease in M_s can be restored through one cycle of postirradiation annealing or aging. They suspect that the inhibition of the martensite transformation is caused by losing long range order under irradiation. Kimura *et al.* [7] confirms Hoshiya's result by differential scanning calorimetry (DSC). What's more, they also confirm the generation of amorphous regions and vacancy clusters using transmission electron microscopy (TEM). Besides amorphization and disordering, Kimura *et al.* also think that irradiation-induced stress may play a role in the suppression of the martensite transformation. Matsukawa *et al.* [10] conduct a similar study as Kimura *et al.* and find that the $B2$-$B19'$ transformation can be completely suppressed under certain irradiation conditions due to amorphization. Later, Konopleva *et al.* [9] found that neutron irradiation not only lowers the M_s, but also changes the transformation path from a one-step transformation ($B2 \rightarrow B19'$) to a two-step transformation ($B2 \rightarrow R \rightarrow B19'$) due to irradiation disordering. Belyaev *et al.* [11] concur that irradiation amorphization changes the path of transformation, and additionally finds that neutron irradiation can induce the $B19' \rightarrow B2$ phase transformation without applied stress [12].

Most proton irradiations [13–22] show similar effects on the M_s as neutron irradiation. Al-Aql and co-workers [13,14,16] consider that point defects play a significant role in the suppression of the martensite transformation, while Dughaish [15] purports the suppression to be a synergistic effect of both point defect pinning and disordering. Wang *et al.* [17] show that proton irradiation does not affect the R phase transformation but lowers both M_s/M_f and A_s/A_f ratios; they ascribe these behaviors to the formation of TiH and TiH_2. Contrary to Konopleva's neutron irradiation study, wherein irradiation induces the path change from $B2 \rightarrow B19'$ to $B2 \rightarrow R \rightarrow B19'$, Gao *et al.* [21] find that proton irradiation induces the path change from $B2 \rightarrow R \rightarrow B19'$ to $B2 \rightarrow B19'$ due to irradiation-induced stresses. Zhao *et al.* [22] observe a decrease in M_s in the one-step transformation but attribute it to irradiation-induced amorphization and irradiation-induced segregation. Most ion irradiations [23–25] cause a decrease in M_s, for similar reasons as neutron irradiation. Finally, Wang and co-workers' electron irradiation studies show a decrease of M_s when the dose rate is high [26], but nearly no influence on M_s when the dose rate is low [27].

The aforementioned literature focuses on thermal-induced martensite transformations, but irradiation effects are also studied on stress-induced martensite transformations. Afzal *et al.* [18] investigate the stress-induced martensite transformation under proton irradiation and find that irradiation suppresses the one-step transformation but prompts the two-step transformation. Stresses required to initiate the R-phase transformation and martensite transformation decrease with increasing irradiation exposure time and may be associated with disordering. Ayub *et al.* [19] observe the same effect

---

*Corresponding author: chalyoung@outlook.com on the one-step transformation for irradiation temperatures of 25 °C and 50 °C. But higher irradiation temperatures, specifically 75 °C and 100 °C, change the transformation path from a two-step to a one-step transformation, due to irradiation-induced Ni_4Ti_3 segregation.

This review of the experimental literature reveals a lack of a unified explanation of irradiation effects on thermal- and stress-induced martensite transformations. This apparent controversy stems from the nature of irradiation experiments, in which varying just a single experimental parameter (e.g., temperature, dose, dose rate, irradiating particle type) produces changes to the nature (or existence) of the irradiation damage cascade and the resultant defects. A wide variety of defect types are produced by irradiation in NiTi, ranging from point defects and chemical disordering (e.g., antisite defects) [28,29] to extended defects such as dislocation loops and amorphous regions [29,30]. These various defects often exist concurrently in materials examined *post mortem* after irradiation, and are likely to have synergetic effects on the martensitic transformation through several mechanisms, including stress relaxation, grain boundary pinning, or disordering. These synergetic behaviors preclude researchers from drawing clear conclusions about the fundamental roles of individual defect types on the martensitic transformation.

Fortuitously, simulations may help solve this problem of multiple dependent variables, since each microstructural factor can be introduced individually. Molecular dynamics (MD) simulations can successfully explain both thermal-induced [31–48] and stress-induced [33,37,43,49–74] martensite transformations in NiTi. Most of the published MD simulations on martensite transformations in NiTi are focused on perfect single crystals, polycrystals, or crystals containing "annealing twin" boundaries. The role of irradiation type defects—e.g., amorphization, chemical segregation, and especially point defects—on NiTi transformations remains underexplored by MD. Local stresses are the focus of a few studies. For example, Chowdhury *et al.* [51] used MD to prove that the existence of coherent Ti_4Ni_3 precipitates can reduce the stress needed to initiate the $B2 \rightarrow B19'$ transformation due to the stress field around the precipitate. Similarly, Ko *et al.* [72] and Zhang *et al.* [66] show that amorphous regions suppress thermal- and stress-induced $B19'$ formation by changing local stress. With respect to defects, Tehrani *et al.* [34] show that both vacancy and antisite point defects inhibit thermal-induced martensite transformation, with antisite point defects having a more obvious effect than vacancies.

In this paper, the effect of different types of point defects—namely interstitials, vacancies, vacancy clusters, and antisite point defects—on the stress-induced martensite transformation is studied using MD. This work focuses specifically on the one-step $B2 \rightarrow B19'$ transformation, given the lack of interatomic potentials that can accurately describe the two-step martensite transformation. This work will show that all defect types inhibit the stress-induced martensite transformation, though each to a differing degree. The specific mechanism is the synergistic defect-driven grain boundary pinning and disordering.

II. SIMULATION METHODS

A modified embedded atom method (MEAM) potential developed by Ko *et al.* [37] is used in this simulation of equiatomic NiTi. This potential is widely used by researchers to study both thermal-induced [37,49] and stress-induced [55,57–60,62,64,66–68,70–74] martensite transformations. Moreover, this potential is intentionally developed to capture the phase transformations between the $B2$ and $B19\prime$ structures in equiatomic NiTi alloy with high predictive accuracy and is by far the most widely used potential for stress-induced martensite transformation in NiTi.

ATOMSK [75] is used to build the initial microstructures of the simulation cell. The dimensions of the simulation cell are $21.2 \times 21.2 \times 21.0$ nm in the x, y, and z directions respectively (representing $50 \times 50 \times 70$ unit cells with lattice constant of 3 Å), with x parallel to $[1\bar{1}0]_{bcc}$, y parallel to $[110]_{bcc}$, and z parallel to $[001]_{bcc}$. Ordered $B2$ (CsCl) structure is built with Ti occupying the corner of the bcc cell, and Ni occupying the body centered position. Five unique simulation cells are built. The first simulation cell has a perfect $B2$ single crystal and is henceforth set as the reference simulation. The second and third simulation cells are $B2$ single crystals with randomly distributed vacancies at a concentration of 10^{-4} and 10^{-3} (at. %), respectively. The purpose of the third simulation is not to introduce individual vacancies, but rather to investigate vacancy clusters through later simulated annealing. The fourth and fifth simulation cells are $B2$ single crystals with randomly distributed interstitials and antisite point defects, respectively, at concentrations of 10^{-4} (at. %). The second through fifth simulations will be referred to as the vacancy simulation, vacancy cluster simulation, interstitial simulation, and antisite simulation henceforth for convenience. (Note that interstitial clusters and antisite clusters are not simulated because these clusters are not found experimentally.) The point defect concentrations used in the simulations are intentionally higher than experimentally achievable (even under extreme irradiation fluences), so that the deformation phenomena will be distinctly obvious [34]. Another key simplification is that all point defects are generated stoichiometrically (i.e., 50% of Ti and 50% Ni), while in reality, Ni vacancies and Ti antisites are more energetically favorable than Ti vacancies and Ni antisites and will thus be present at a higher concentration [76,77]. But this approach enables us to eliminate the influence of chemical composition, which can drastically affect the martensite transformation behavior [31,36].

A periodic boundary condition is applied in all three dimensions, meaning that the simulations do not have a free surface. The simulation cells are first equilibrated under NPT conditions (constant atom number, pressure, and temperature) using a time step size of 0.002 ps for 100 ps in vacuum at 400 K, which is approximately 20 K higher than the M_s temperature of the potential used [37]. The strain-controlled method is used during the deformation. The crystal is loaded in the z direction, with strain rate of 0.001 ps^{-1}, until a total strain of 0.1 (50 000 steps), which is the limit of recoverable strain for NiTi [53,58,63], and then the deformation is reversed until the strain returns to 0 (100 000 steps). No stress is applied along the x or y directions, which are allowed to relax during the deformation. The time step size during the deformation is also 0.002 ps. The open-source code LAMMPS [78] is used to perform the simulations, and open-source software OVITO is used for visualization [79], during which the common neighbor analysis (CNA) method is used to determine the phases present. The CNA algorithm is proven to be efficient at capturing the $B2 \rightarrow B19'$ transformation when using Ko's potential [55,57–60,62,64,66–68,70–74].

III. RESULTS

Figures 1(a)–1(e) show the equilibrized simulation boxes of the reference, vacancy, vacancy cluster, and interstitial and antisite simulation, respectively. The equilibrized material is predominantly an ordered $B2$ single crystal. However, atoms adjacent to vacancies and interstitials are off ideal lattice sites due to stress induced by that vacancy or interstitial, and their lattice type is hence referred to as "other." Antisite defects do not cause lattice structure changes when using the CNA algorithm. No $B19'$ structure exists before deformation. Cluster analysis of Figs. 1(b)–1(d) shows that both point defect species tend to exist as individual defects at concentrations of 10^{-4}, but form into clusters at concentrations of 10^{-3} after equilibration.

Figure 2 shows the stress as a function of time (i.e., stress-strain curve) and fraction of $B19'$ phase as a function of time, for the reference simulation. Insets show the $B19'$ phase surfaces at certain points, to illustrate the phase evolution throughout the loading and unloading. The stress is higher than measured experimentally due to the high strain rate used in MD, and it is consistent with other MD simulations using the Ko potential [55,57–60,62,64,66–68, 70–74]. The deformation can be subdivided into several stages. First, for time steps 0–15 000, elastic deformation of the $B2$ phase occurs during loading since no $B19'$ has yet formed at this stage. The slope of the stress-time curve is constant, indicative of the constant elastic modulus. The second stage of deformation is characterized by a slope change near time step ~15 000, which indicates the onset of the $B2 \rightarrow B19'$ transformation since the transformation induces local contraction due to differences in $B2$ and $B19'$ lattice parameter. In the third deformation stage, the slope of the stress-time curve continually changes as the time step increases from 20 000 to 50 000, indicating formation of new $B19'$ grains and coalescence of existing $B19'$ grains. In the fourth stage, spanning between time steps 50 000 and 85 000, the reverse transformation occurs, with $B19'$ reverting back to $B2$. Finally, between time steps 90 000 and 100 000, elastic recovery of the $B2$ phase occurs during unloading. The curves are not symmetrical, indicating that hysteresis happens during loading and unloading. However, hysteresis is beyond the scope of the present study because it is more appropriate to use a stress-controlled simulation to study hysteresis.

Figures 3(a) and 3(b) show the stress-time curves for all of the simulations and Figs. 3(c) and 3(d) show the $B19'$-time steps curves for all of the simulations. The most significant differences across the simulations happen between time steps 10 000 and 30 000, and this range is therefore magnified to show detail in Figs. 3(b) and 3(d). One can see in Fig. 3(b) that the interstitial simulation has the highest stress between time steps 10 000 and 15 000, while the vacancy cluster simulation has the lowest stress. The other simulations show little difference over this time step range. Stress-time slope changes occur near time step 15 000, indicating the onset of the martensite transformation, which is confirmed by the increase in $B19'$ phase fraction shown in Fig. 3(d). The degree of stress-time slope change across the simulations trends

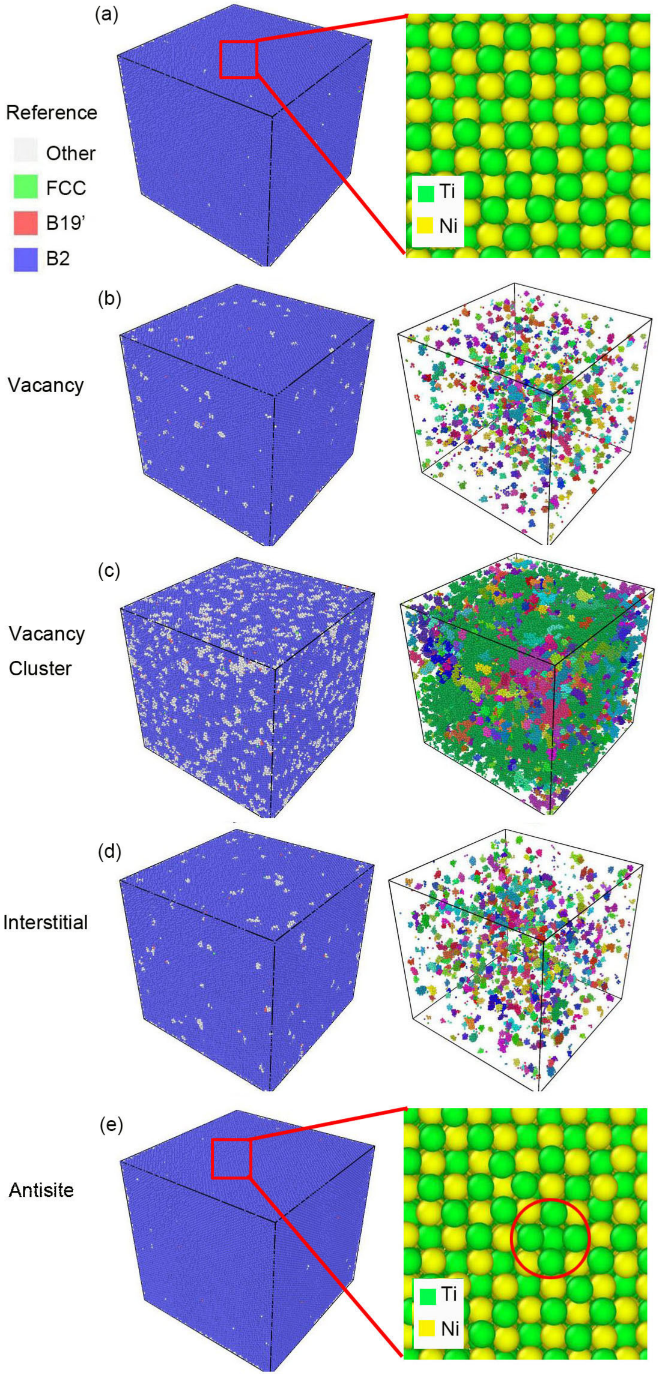

FIG. 1. Equilibrized simulation boxes of (a) reference, (b) vacancy, (c) vacancy cluster, (d) interstitial and (e) antisite simulations, with insets showing chemical composition in (a) and (e), and clusters of atoms identified as having another lattice type in (b)–(d).

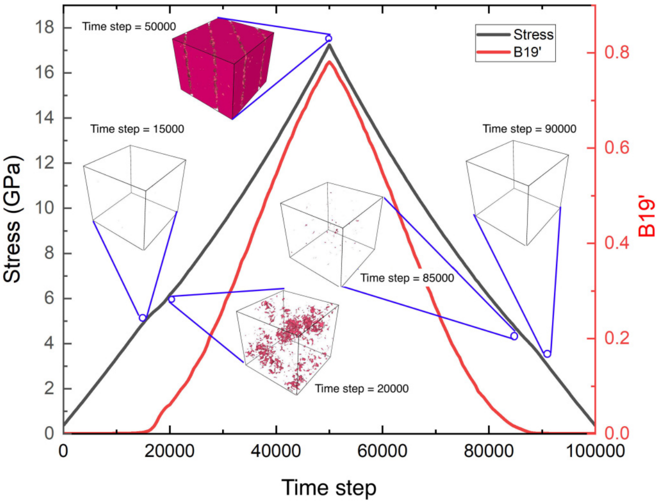

FIG. 2. Stress and $B19'$ phase fraction as a function of time step for the reference simulation; insets show the evolution of the $B19'$ phase at selected points throughout the loading and unloading.

as vacancy clusters < interstitials < vacancies < antisite < reference.

Because a slope change indicates the $B2 \rightarrow B19'$ transformation, the larger the slope change, the greater the extent of the martensite transformation. What's more, the defects also cause an increase in the strain required to initiate the martensite transformation, as shown in Fig. 3(e), which is taken at a fixed $B19'$ phase fraction of 0.02 for consistent comparison across simulations. The strain at the onset of the transformation follows the opposite trend as the stress-time curve slope change: reference < antisite < vacancies < interstitials < vacancy clusters.

From Fig. 3(b), we can see that all types of point defects studied inhibit the $B2 \rightarrow B19'$ transformation. At a fixed point defect concentration of 10^{-4}, interstitials have the most pronounced effect, while antisite defects have the least pronounced effect. This trend is notably different from that in thermal-induced martensite transformations [34], wherein antisite defects have a stronger influence than vacancies. Increasing the vacancy concentration by one order of magnitude to initiate vacancy clustering drastically inhibits the $B2 \rightarrow B19'$ transformation.

Figure 4 shows the still frames from each of the simulations, showing the phase evolution throughout the loading and unloading process, taken at fixed time steps; the same color coding is used as in the legend in Fig. 1. These still frames reveal how significantly the vacancy clusters inhibit the $B2 \rightarrow B19'$ transformation compared to the other defect types. Visually, the still frames from the reference, vacancy, interstitial, and antisite simulations are difficult to distinguish from one another, which is consistent with quantitative results shown in Fig. 3. Lüders bands form in all simulations except the vacancy cluster simulation; this phenomenon is believed to be associated with low defect levels [80].

Figure 5 shows a two-dimensional slice taken from the vacancy cluster simulation approaching and at the maximum loading. The slice shows only "other" atoms (recall they are identified as "other" because they are off-ideal lattice sites due to relaxation around vacancy clusters) and the surface of $B19'$ phases. Comparing the magenta boxed region across all time steps reveals that the $B19'$ phases tend to nucleate in regions between vacancy clusters, and also that the vacancy clusters can pin the $B19'$ interfaces during their growth. Complementary slice analysis of the other simulations is not shown because the lower concentration of point defects limits the number of defects a given slice can intersect, thus identifying a "representative" slice is unrealistic.

IV. DISCUSSION

The observed suppression of the martensitic transformation is likely due to the defect species introduced into the original simulation boxes, because the kinetics of dynamic precipitation or amorphous region formation cannot be reached in MD time scales. Existing theories on how point defects inhibit the $B2 \rightarrow B19'$ transformation include (1) point defects—vacancies, to be specific—relax local stresses and thus inhibit the martensite transformation, (2) point defects pin grain boundaries of the $B19'$ phase, making their growth harder, and (3) point defects disrupt long range order, which is critical for the $B2 \rightarrow B19'$ transformation.

The results of this work are contrary to the local stress relaxation theory. That is, vacancies may cause local stress relaxation since the simulation box containing vacancies is less closely packed than the other simulation boxes. However, interstitials will have the opposite effect, since stresses are easier to build up in the interstitial simulation, as shown in Fig. 2(b). So, by the stress relaxation theory argument, interstitials should promote the $B2 \rightarrow B19'$ transformation. But both vacancies and interstitials inhibit the transformation, which may be inconsistent with the local stress relaxation theory.

With respect to the grain boundary pinning idea, vacancies likely pin $B19'$ interfaces from further growth, as shown in Fig. 5. The pinning effect is believed to come from the stress distortion generated by point defects. Interstitials generate a higher stress distortion than vacancies, and antisite defects generate the lowest stress distortion. Thus, the extent of the pinning effect on inhibiting the $B2 \rightarrow B19'$ transformation would likely go in the order of interstitial > vacancy > antisite, just as shown in Fig. 2(d). The higher the vacancy concentration, the higher the pinning force. Thus, the effect of vacancy clusters is more pronounced than that of individual vacancies. But as shown in Fig. 5, the pinning effect is not the only active mechanism, as vacancy clusters not only affect the growth of $B19'$ grains but also the nucleation of $B19'$ grains. Thus, chemical disordering likely plays at least some role in the early stages of the transformation.

Grummon *et al.* [24] shows that ion irradiation-induced chemical disordering can frustrate the forward and reverse displacive shape memory transformations in NiTi thin films, by inhibiting collective shearing. Additionally, Huo *et al.* [81] points out that disordering makes the lattice structure less distinct between the $B2$ and $B19'$ phases, consequently lowering both the chemical potential energy and the coherency energy between the two phases. These effects compete with one another, as a reduction in chemical potential energy promotes the $B2 \rightarrow B19'$ transformation, while a reduction in

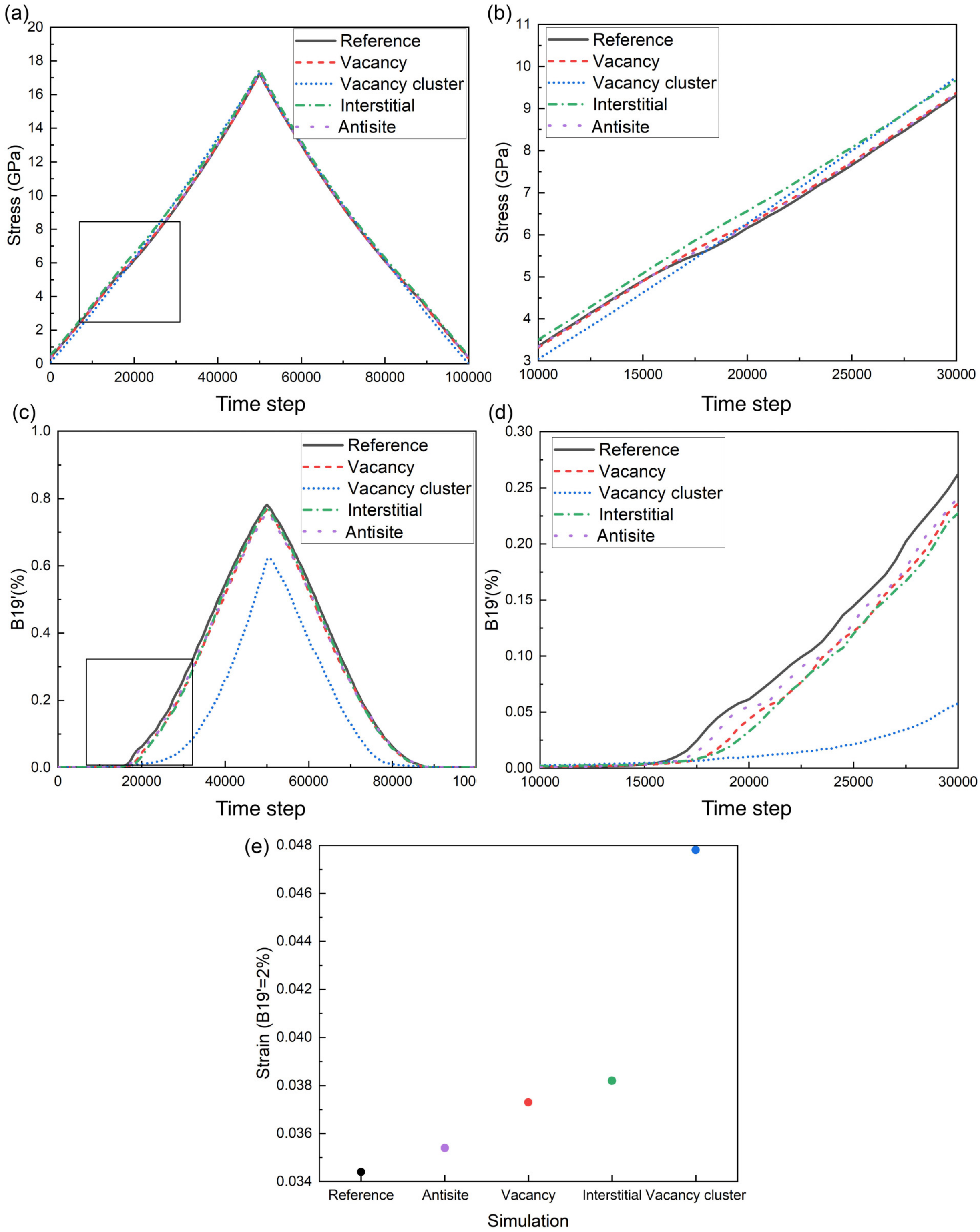

FIG. 3. (a), (b) Stress-time curves and (c), (d) $B19'$-time curves of all the simulations; (b) and (d) show an enlarged view of the framed regions in (a) and (c), respectively; (e) strain required to initiate martensite transformation, taken at $B19'$ phase fraction of 0.02.

coherency limits the transformation. Since the reduction of chemical potential energy by disordering exceeds that of coherency energy, disordering tends to inhibit the $B2 \rightarrow B19'$ transformation.

First-principles calculations of defect formation energies support the idea that irradiation-induced defects (and defects, more generally) suppress the nucleation of $B19'$ grains. Specifically, density functional theory (DFT) calculations reveal that Ni and Ti vacancies [77,82], antisite defects [77,83], and H interstitials [83] are more stable in the $B2$ phase than in the $B19'$ phase. Additionally, Holec and co-workers [83] also show that with increasing H interstitial concentration, the

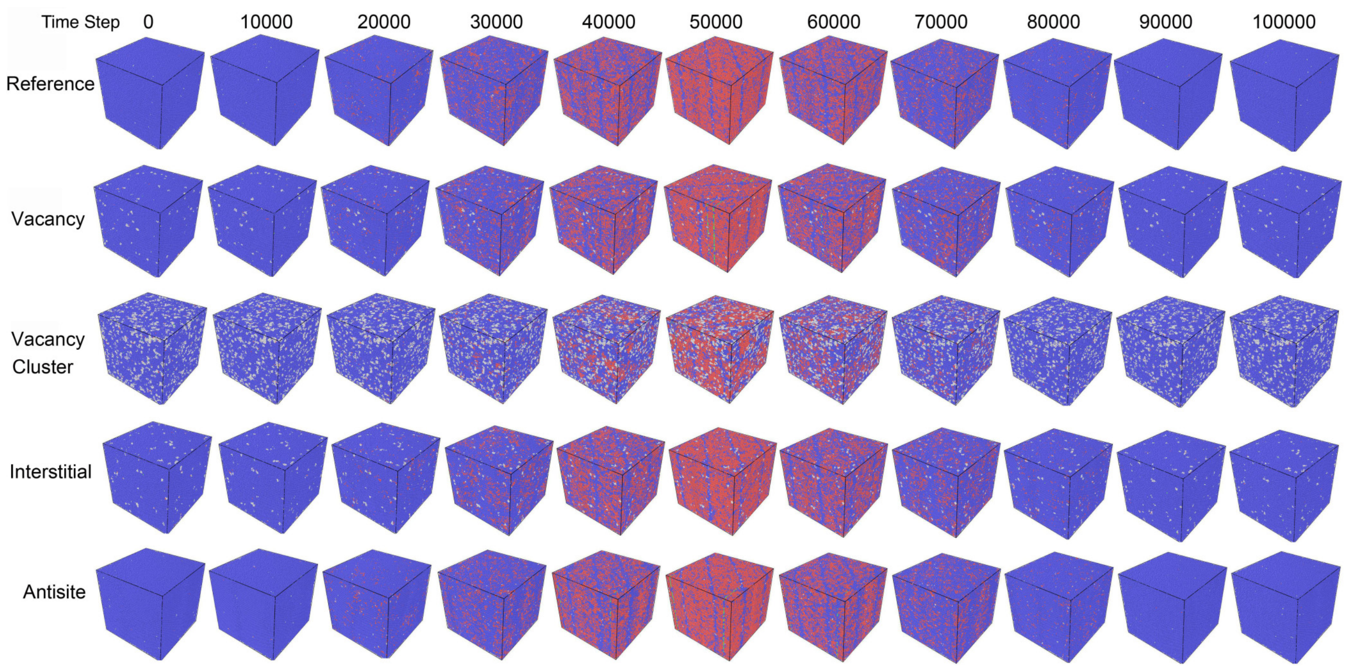

FIG. 4. Snapshots of all the simulations showing phase evolution throughout loading and unloading, at time steps indicated. Colors are identical to those provided in legend in Fig. 1.

total energies of the $B2$ and $B19'$ phases approach one another, which decreases the driving force for thermal-induced martensite transformations. Collectively, these DFT studies suggest that the presence of defects extends the temperature range for $B2$ stability, which supports the findings herein.

V. CONCLUSIONS

Molecular dynamics simulations are used to study the effects of various point defect species on the $B2 \rightarrow B19'$ martensite transformation in NiTi. Results show that all types of defects studied—vacancies, vacancy clusters, interstitials, and antisite defects—inhibit martensite transformations, though each to a differing degree. At a fixed point defect concentration, interstitials have the most pronounced effect on suppressing the extent of the martensite transformation and increasing the strain required to initiate the transformation; by contrast, antisite defects have the smallest effect on suppressing the transformation. Increasing the vacancy concentration by an order of magnitude to induce vacancy clustering greatly

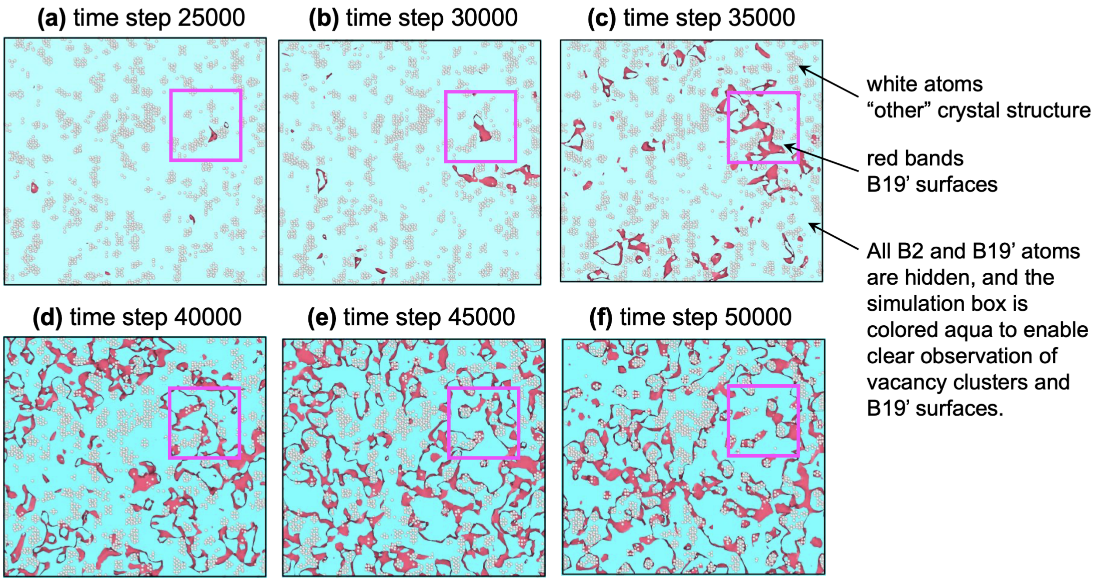
(a) time step 25000
(b) time step 30000
(c) time step 35000
(d) time step 40000
(e) time step 45000
(f) time step 50000

white atoms
"other" crystal structure

red bands
B19' surfaces

All B2 and B19' atoms are hidden, and the simulation box is colored aqua to enable clear observation of vacancy clusters and B19' surfaces.

FIG. 5. Snapshots of vacancy cluster simulation at time steps (a) 25 000, (b) 30 000, (c) 35 000, (d) 40 000, (e) 45 000, and (f) 50 000, showing only the "other" atoms (white atoms, relaxed around vacancy clusters) and $B19'$ surfaces (red). Note that all $B2$ and $B19'$ type atoms are hidden, and the simulation box background is colored aqua, to enable clear observation of the other atoms.

inhibits the extent of the martensite transformation and dramatically increases the martensite initiation strain. Both grain boundary pinning and disordering may act synergistically to explain the inhibition of stress-induced martensite transformations. The extent to which these conclusions translate for real NiTi systems should be considered within the limitations of MD, including strain rate sensitivity, time scales, and typical NiTi precipitate and grain microstructures.

ACKNOWLEDGMENTS

The authors thank Professor P. Anderson, Professor Y. Wang, and Professor M. Mills from The Ohio State University for their engaging scientific discussions. This work was supported by the U.S. Department of Energy, Office of Science, Basic Energy Sciences, under Award No. DE-SC0020150.

---

[1] K. Otsuka and C. M.Wayman, *Shape Memory Materials* (Cambridge University Press, Cambridge, UK, 1999) .

[2] T. W. Duerig, K. N. Melton, and D. W. C. M. Stöckel, Engineering Aspects of Shape Memory Alloys (Butterworth-Heinemann, Oxford, UK, 2013).

[3] M. Nishikawa, T. Narikawa, M. Iwamoto, and K. Watanabe, Conceptual design of a cassette compact toroid reactor (the zero-phase study)—quick replacement of the reactor core, Fusion. Technol. **9**, 101 (1986).

[4] T. Hoshiya, H. Sekino, Y. Matsui, F. Sakurai, and K. Enami, Effects of residual strain on deformation processes of neutron-irradiated TiNi and TiPd shape memory alloys, J. Nucl. Mater. **233-237**, 599 (1996).

[5] T. Hoshiya, F. Takada, Y. Ichihashi, and H-R. Pak, Restoration phenomena of neutron-irradiated TiNi shape memory alloys, Mater. Sci. Eng. A. **130**, 185 (1990).

[6] T. Hoshiya, S. Shimakawa, Y. Ichihashi, M. Nishikawa, and K. Watanabe, Fast neutron irradiation of TiNi shape memory alloys, J. Nucl. Mater. **179-181**, 1119 (1991).

[7] A. Kimura, H. Tsuruga, T. Morimura, S. Miyazaki, and T. Misawa, Effects of post-irradiation annealing on the transformation behavior of Ti–Ni Alloys, Mater. Trans. JIM **34**, 1076 (1993).

[8] T. Hoshiya, M. Ohmi, Y. Matsui, and M. Nishikawa, Shape memory characteristics of neutron irradiated Ti–Ni shape memory alloy couplers, J. Nucl. Mater. **258-263**, 2036 (1998).

[9] R. F. Konopleva, I. V. Nazarkin, V. L. Solovei, V. A. Chekanov, S. P. Belyaev, A. E. Volkov, and A. I. Razov, Influence of neutron irradiation on the martensitic transformations and shape-memory effect in a TiNi alloy, Phys. Solid State **40**, 1550 (1998).

[10] Y. Matsukawa, T. Suda, S. Ohnuki, and C. Namba, Microstructure and mechanical properties of neutron irradiated TiNi shape memory alloy, J. Nucl. Mater. **271-272**, 106 (1999).

[11] S. P. Belyaev, A. E. Volkov, R. F. Konopleva, I. V. Nazarkin, A. I. Razov, V. L. Solovei, and V. A. Chekanov, Kinetics of radiation damage and martensitic transformations in TiNi alloys irradiated with neutrons, Phys. Solid State **43**, 2158 (2001).

[12] S. P. Belyaev, R. F. Konopleva, I. V. Nazarkin, A. I. Razov, V. L. Soloveĭ, and V. A. Chekanov, Neutron-irradiation-induced shape memory effect in a TiNi alloy, Phys. Solid State **49**, 1969 (2007).

[13] A. A. Al-Aql, Z. H. Dughaish, and M. R. Baig, Study of the martensitic transformation in shape-memory Nitinol proton-irradiated alloy by electrical resistivity measurements, Mater. Lett. **17**, 103 (1993).

[14] A. A. Al-Aql and Z. H. Dughaish, Effect of energy variation of proton beam on sharpening nitinol electrical resistivity increase at the martensitic transformation, Phys. B: Condens. Matter **229**, 91 (1996).

[15] Z. H. Dughaish, Effect of variation of proton beam energy on the martensitic transformation temperature of shape memory nitinol alloy, Mater. Lett. **32**, 29 (1997).

[16] A. A. Al-Aql, Study of the influence of proton irradiation on the transformation temperature of Nitinol by electrical resistivity measurements, Phys. B: Condens. Matter **239**, 345 (1997).

[17] Z. G. Wang, X. Zu, Y. Q. Fu, J. H. Wu, and H. J. Du, Effects of proton irradiation on transformation behavior of TiNi shape memory alloy thin films, Thin. Solid. Films **474**, 322 (2005).

[18] N. Afzal, I. M. Ghauri, F. E. Mubarik, and F. Amin, Mechanical response of proton beam irradiated nitinol, Phys. B: Condens. Matter **406**, 8 (2011).

[19] R. Ayub, N. Afzal, and R. Ahmad, Phase transformation studies in unirradiated and proton beam irradiated Ni–Ti alloy between 25 and 100 °C, Philos. Mag. **92**, 2164 (2012).

[20] Z. H. Dughaish, Effect of proton irradiation on some physical properties of nitinol (NiTi) shape memory alloy: A review. Arab, J. Sci. Eng. **39**, 511 (2014).

[21] Z. Y. Gao, H. Z. Wang, Y. Y. Zhu, X. L. Meng, and W. Cai, The martensitic transformation of Ti–Ni shape memory thin films under proton irradiation, Thin. Solid. Films **584**, 369 (2015).

[22] Y. Zhao, R. Ning, X. Yi, Z. Gao, H. Wang, and W. Cai, Formation of multilayer structure and evolution of shape recovery characteristics in proton irradiated TiNi alloy thin films, Mater. Charact. **164**, 110348 (2020).

[23] A. Barbu, A. Dunlop, A. Hardouin Duparc, G. Jaskierowicz, and N. Lorenzelli, Microstructural modifications induced by swift ions in the NiTi intermetallic compound, Nucl. Instrum. Methods Phys. Res. B **145**, 354 (1998).

[24] D. S. Grummon and R. Gotthardt, Latent strain in titanium–nickel thin films modified by irradiation of the plastically-deformed martensite phase with 5 MeV Ni^{2+}, Acta Mater. **48**, 635 (2000).

[25] T. B. Lagrange and R. Gotthard, Microstructural evolution and thermo-mechanical response of Ni ion irradiated TiNi SMA thin films, J. Optoelectron. Adv. Mater. **5**, 313 (2003).

[26] Z. G. Wang, X. T. Zu, Y. Huo, S. Zhu, X. W. Wei, and L. M. Wang, Effect of electron irradiation and heat treatment on the multi-step transformation in a Ni-rich near-equiatomic TiNi alloy, Nucl. Instrum. Methods Phys. Res. B **215**, 436 (2004).

[27] Z. G. Wang, X. T. Zu, Y. Q. Fu, S. Zhu, and L. M. Wang, Electron irradiation effect on the reverse phase transformation temperatures in TiNi shape memory alloy thin films, Nucl. Instrum. Methods Phys. Res. B **227**, 337 (2005).

[28] D. F. Pedraza and L. K. Mansur, The effect of point defects on the amorphization of metallic alloys during ion

implantation, Nucl. Instrum. Methods Phys. Res. B **16**, 203 (1986).

[29] L. Huang, K. Ma, L. T. Belkacemi, M. Loyer-Prost, E. Meslin, E. Toijer, L. Messina, C. Domain, J. Vidal, and M. Nastar, Impact of the local microstructure fluctuations on radiation-induced segregation in dilute Fe-Ni and Ni-Ti model alloys: A combined modeling and experimental analysis, Acta Mater. **225**, 117531 (2022).

[30] V. Poltavtseva, A. Larionov, and G. Zheltova, Peculiarities of structure and hardening of Ni-Ti alloy surface layers formed by $_{84}\mathrm{Kr}^{15+}$ ions irradiation at 147 MeV energy at high temperatures, IOP Conf. Ser.: Mater. Sci. Eng. **168**, 012032 (2017).

[31] H. Ishida and Y. Hiwatari, MD simulation of martensitic transformations in TiNi alloys with MEAM, Mol. Simul. **33**, 459 (2007).

[32] D. Mutter and P. Nielaba, Simulation of the thermally induced austenitic phase transition in NiTi nanoparticles, Eur. Phys. J. B **84**, 109 (2011).

[33] Y. Zhong, K. Gall, and T. Zhu, Atomistic characterization of pseudoelasticity and shape memory in NiTi nanopillars, Acta Mater. **60**, 6301 (2012).

[34] A. M. Tehrani, H. Shahrokhshahi, N. Parvin, and J. Brgoch, Influencing the martensitic phase transformation in NiTi through point defects, Int. J. Appl. Phys. **118**, 014901 (2015).

[35] S. Qin, J. Shang, X. Wang, and F. Wang, Effects of $B2/B19'$ phase boundary on thermally induced phase transition in NiTi: An atomistic study, Appl. Surf. Sci. **353**, 1052 (2015).

[36] J. Frenzel, A. Wieczorek, I. Opahle, B. Maaß, R. Drautz, and G. Eggeler, On the effect of alloy composition on martensite start temperatures and latent heats in Ni–Ti-based shape memory alloys, Acta Mater. **90**, 213 (2015).

[37] W. Ko, B. Grabowski, and J. Neugebauer, Development and application of a Ni-Ti interatomic potential with high predictive accuracy of the martensitic phase transition, Phys. Rev. B **92**, 134107 (2015).

[38] C. Kexel, S. Schramm, and A. V. Solov'yov, Atomistic simulation of martensite-austenite phase transition in nanoscale nickel-titanium crystals, Eur. Phys. J. B **88**, 221 (2015).

[39] G. Ren and H. Sehitoglu, Interatomic potential for the NiTi alloy and its application, Comput. Mater. Sci. **123**, 19 (2016).

[40] S. Gur and G. N. Frantziskonis, Linking simulations and experiments for the multiscale tracking of thermally induced martensitic phase transformation in NiTi SMA, Model. Simul. Mater. Sci. Eng. **24**, 075006 (2016).

[41] G. Ma, S. Qin, J. Shang, F. Wang, and Y. Chen, Atomistic study on the phase transformation in NiTi under thermal cycling, J. Alloys Compd. **705**, 218 (2017).

[42] S. Gur, V. R. Manga, S. Bringuier, K. Muralidharan, and G. N. Frantziskonis, Evolution of internal strain in austenite phase during thermally induced martensitic phase transformation in NiTi shape memory alloys, Comput. Mater. Sci. **133**, 52 (2017).

[43] M. Muralles, S. Park, S. Y. Kim, and B. Lee, Phase transformations, detwinning and superelasticity of shape-memory NiTi from MEAM with practical capability, Comput. Mater. Sci. **130**, 138 (2017).

[44] S. Qin, J. Shang, F. Wang, and Y. Chen, Symmetrical tilt grain boundary engineering of NiTi shape memory alloy: An atomistic insight, Mater. Des. **137**, 361 (2018).

[45] J. Wan, Z. Chen, S. Qin, and J. Shang, Effect of hydrostatic pressure on thermally induced phase transformation in NiTi alloy: A molecular dynamics study, Comput. Mater. Sci. **153**, 119 (2018).

[46] Z. Chen, S. Qin, J. Shang, F. Wang, and Y. Chen, Size effects of NiTi nanoparticle on thermally induced martensitic phase transformation, Intermetallics **94**, 47 (2018):.

[47] R. I. Babicheva, A. S. Semenov, S. V. Dmitriev, and K. Zhou, Effect of grain boundary segregations on martensitic transformation temperatures in NiTi bi-crystals, Lett. Mater. **9**, 162 (2019).

[48] W. Ko, B. Grabowski, and J. Neugebauer, Impact of asymmetric martensite and austenite nucleation and growth behavior on the phase stability and hysteresis of freestanding shape-memory nanoparticles, Phys. Rev. Mater. **2**, 030601 (2018).

[49] R. S. Elliott, N. Triantafyllidis, and J. A. Shaw, Reversible stress-induced martensitic phase transformations in a bi-atomic crystal, J. Mech. Phys. Solids. **59**, 216 (2011).

[50] D. Mutter and P. Nielaba, Simulation of the shape memory effect in a NiTi nano model system, J. Alloys Compd. **577**, S83 (2013).

[51] P. Chowdhury, L. Patriarca, G. Ren, and H. Sehitoglu, Molecular dynamics modeling of NiTi superelasticity in presence of nanoprecipitates, Int. J. Plast. **81**, 152 (2016).

[52] S. Alkan and H. Sehitoglu, Dislocation core effects on slip response of NiTi-a key to understanding shape memory, Int. J. Plast. **97**, 126 (2017).

[53] B. Wang, G. Kang, Q. Kan, K. Zhou, and C. Yu, Molecular dynamics simulations to the pseudo-elasticity of NiTi shape memory alloy nano-pillar subjected to cyclic compression, Comput. Mater. Sci. **131**, 132 (2017).

[54] Y. Guo, X. Zeng, H. Chen, T. Han, H. Tian, and F. Wang, Molecular dynamics modeling of the effect of nanotwins on the superelasticity of single-crystalline NiTi alloys, Adv. Mater. Sci. Eng. 2017 (2017).

[55] W. Ko, S. B. Maisel, B. Grabowski, J. B. Jeon, and J. Neugebauer, Atomic scale processes of phase transformations in nanocrystalline NiTi shape-memory alloys, Acta Mater. **123**, 90 (2017).

[56] X. Chen, S. Lu, Y. Zhao, T. Fu, C. Huang, and X. Peng, Molecular dynamic simulation on nano-indentation of NiTi SMA, Mater. Sci. Eng. A. **712**, 592 (2018).

[57] B. Wang, G. Kang, Q. Kan, W. Wu, K. Zhou, and C. Yu, Atomistic study on the super-elasticity of single crystal bulk NiTi shape memory alloy under adiabatic condition, Comput. Mater. Sci. **142**, 38 (2018).

[58] B. Wang, G. Kang, Q. Kan, W. Wu, K. Zhou, and C. Yu, Atomistic study on the super-elasticity of nanocrystalline NiTi shape memory alloy subjected to a cyclic deformation, Comput. Mater. Sci. **152**, 85 (2018).

[59] P. Srinivasan, L. Nicola, and A. Simone, Atomistic modeling of the orientation-dependent pseudoelasticity in NiTi: Tension, compression, and bending, Comput. Mater. Sci. **154**, 25 (2018).

[60] Y. A. Baimova, S. V. Dmitriev, N. N. Kuranova, R. R. Mulyukov, A. V. Pushin, and V. G. Pushin, Molecular dynamics study of the deformation processes of metallic materials in structural and phase (martensitic) transformations, Phys. Met. Metallogr. **119**, 589 (2018).

[61] M. Wang, S. Jiang, and Y. Zhang, Phase transformation, twinning, and detwinning of NiTi shape-memory alloy subject to a

shock wave based on molecular-dynamics simulation, Materials **11**, 2334 (2018).

[62] H. Lu, C. Chen, and N. Tsou, The analysis of superelasticity and microstructural evolution in NiTi single crystals by molecular dynamics, Materials **12**, 57 (2019).

[63] X. Chen, W. Chen, Y. Ma, Y. Zhao, C. Deng, X. Peng, and T. Fu, Tension-Compression asymmetry of single-crystalline and nanocrystalline NiTi shape memory alloy: An atomic scale study, Mech. Mater. **145**, 103402 (2020).

[64] Z. Chen, J. Shang, and Y. Chen, Shear deformation behavior of the austenitic Σ3 {1 1 2} twin boundary in NiTi shape memory alloy: An atomistic study, Appl. Surf. Sci. **509**, 145318 (2020).

[65] B. Wang, G. Kang, W. Wu, K. Zhou, Q. Kan, and C. Yu, Molecular dynamics simulations on nanocrystalline super-elastic NiTi shape memory alloy by addressing transformation ratchetting and its atomic mechanism, Int. J. Plast. **125**, 374 (2020).

[66] Y. Zhang, S. Jiang, and M. Wang, Atomistic investigation on superelasticity of NiTi shape memory alloy with complex microstructures based on molecular dynamics simulation, Int. J. Plast. **125**, 27 (2020).

[67] Y. Li, X. Zeng, and F. Wang, Investigation on the micro-mechanism of martensitic transformation in nanopolycrystalline NiTi shape memory alloys using molecular dynamics simulations, J. Alloys Compd. **821**, 153509 (2020).

[68] B. Li, Y. Shen, and Q. An, Structural origin of reversible martensitic transformation and reversible twinning in NiTi shape memory alloy, Acta Mater. **199**, 240 (2020).

[69] B. Wang, G. Kang, C. Yu, B. Gu, and W. Yuan, Molecular dynamics simulations on one-way shape memory effect of nanocrystalline NiTi shape memory alloy and its cyclic degeneration, Int. J. Mech. Sci. **211**, 106777 (2021).

[70] K. Nie, M. Li, W. Wu, and Q. Sun, Grain size-dependent energy partition in phase transition of NiTi shape memory alloys studied by molecular dynamics simulation, Int. J. Solids Struct. **221**, 31 (2021).

[71] W. Ko and J. B. Jeon, Atomistic simulations on orientation dependent martensitic transformation during nanoindentation of NiTi shape-memory alloys, Comput. Mater. Sci. **187**, 110127 (2021).

[72] W. Ko, W. S. Choi, G. Xu, P. Choi, Y. Ikeda, and B. Grabowski, Dissecting functional degradation in NiTi shape memory alloys containing amorphous regions via atomistic simulations, Acta Mater. **202**, 331 (2021).

[73] J. Lee and Y. C. Shin, Molecular dynamics study of bulk properties of polycrystalline NiTi, Metals **11**, 1237 (2021).

[74] Z. Song, X. Tang, X. Chen, T. Fu, H. Zheng, and S. Lu, Nanoindentation and nano-scratching of pure nickel and NiTi shape memory alloy thin films: An atomic-scale simulation, Thin. Solid. Films **736**, 138906 (2021).

[75] P. Hirel, Atomsk: A tool for manipulating and converting atomic data files, Comput. Phys. Commun. **197**, 212 (2015).

[76] A. Baturin, A. Lotkov, V. Grishkov, and A. Lider, Formation of vacancy-type defects in titanium nickelide, MATEC Web Conf. **33**, 03017 (2015).

[77] B. Yue, Y. Li, and F. Zhang, The effect of vacancy on the phase stability of TiNi shape memory alloy from first-principle calculation, Mater. Sci. Forum **687**, 528 (2011).

[78] S. Plimpton, Fast parallel algorithms for short-range molecular dynamics, J. Comput. Phys. **117**, 1 (1995).

[79] A. Stukowski, Visualization and analysis of atomistic simulation data with OVITO–the Open Visualization Tool, Model Simul. Mater. Sci. Eng. **18**, 015012 (2009).

[80] G. Tan, Y. Liu, P. Sittner, and M. Saunders, Lüders-like deformation associated with stress-induced martensitic transformation in NiTi, Scr. Mater. **50**, 193 (2004).

[81] Y. Huo, X. T. Zu, A. Li, Z. G. Wang, and L. M. Wang, Modeling and simulation of irradiation effects on martensitic transformations in shape memory alloys, Acta Mater. **52**, 2683 (2004).

[82] J. M. Lu, Q. M. Hu, L. Wang, Y. J. Li, D. S. Xu, and R. Yang, Point defects and their interaction in TiNi from first-principles calculations, Phys. Rev. B **75**, 094108 (2007).

[83] D. Holec, M. Friák, A. Dlouhý, and J. Neugebauer, Ab initio study of point defects in NiTi-based alloys, Phys. Rev. B **89**, 014110 (2014).